Precision Engineering 72 (2021) 259–271

Contents lists available at ScienceDirect

Precision Engineering

journal homepage: www.elsevier.com/locate/precision

Design of a compliant load cell with adjustable stiffness

M. Smreczak [a,*], L. Rubbert [b], C. Baur [a]

[a] Instant-Lab, École Polytechnique Fédérale de Lausanne (EPFL), Rue de La Maladière 71b, CH-2000, Neuchatel, Switzerland
[b] INSA de Strasbourg, 24 Bld de La Victoire, 67084, Strasbourg, France

ARTICLE INFO

Keywords:
Compliant mechanism
Load cell
Micromanipulation
Adjustable stiffness
Precise force sensing
Zero stiffness
Flexure

ABSTRACT

Manipulation at the sub-micron scale often requires force-sensing capabilities of milli-to nanonewton forces. This article presents a novel design of a compliant load cell with mechanically adjustable stiffness. The system enables adapting force sensitivity to the requirements of a specific application. The principle of the stiffness adjustment is based on a preloaded spring, that stores the potential energy used to compensate the effort needed to deflect the compliant structure of the load cell. Unlike Micro-Electro-Mechanical Systems (MEMS), the new mechanism can be fabricated at the centimeter-scale. This reduces the fragility of the system and facilitates interchange of end-effectors. A main advantage of this solution is the possibility to use one common force sensing device for diverse applications at various scales, such as in biotechnology, semiconductor nanoprobing or microassembly. We describe the analytical model of the load cell and use it to simulate the performance of the stiffness adjustment mechanism. The analytical results are then validated by finite element method (FEM) and experiments performed on a large-scale stainless-steel prototype. Empirical results show that the overall stiffness can be tuned to near-zero and beyond, resulting in a bistable mode. The presented model brings freedom for designing the sensitivity adjustment, and the experimental part shows the ability to reduce the stiffness of the prototype by approximately 200-fold, achieving a force sensing resolution of 0.41 μN

1. Introduction

1.1. Force sensing at small scales

Precise force sensing and control for manipulation at the sub-micron level is required in many areas such as high-end weighing scales, cell manipulation [1] microsurgery [2], microassembly [3] and in the semiconductor industry [4]. Force sensing becomes crucial at the small scale, where visual assessment is limited and contact forces and dynamics become predominant [5]. Scaling laws exemplify those effects negligible at the macroscopic level as critical at the micrometer scale, and vice versa [6]. Surface forces, such as van der Waals, capillary and electrostatic forces, become superior to gravity at smaller scales. These forces, being attractive or repulsive, may dominate the process of contact between a probe and a sample [7]. Reliable modeling of all phenomena that may occur at the small scale is difficult; therefore, semi-automated control of micromanipulation to assist the human operator is highly desired. In some applications, visual feedback is possible and sufficient for teleoperation (e.g. Refs. [8,9]) but in others, force measurement is inevitable for determining physical interactions between objects.

Manipulation typically takes place under an optical microscope at the micron scale, while inside the scanning electron microscope (SEM) at the nanoscale. A commonly used approach involves micromanipulators that are universal platforms, which enable movement of an attached end-effector over several degrees-of-freedom (DoF). A schematic presenting a typical configuration of a micromanipulator used for force sensing at small scales is presented in Fig. 1. Although numerous examples of force sensing devices can be found in the literature and on the market, a sensor offering adjustable sensitivity and easily interchangeable end-effectors is not available. Indeed, adaptation of the force sensitivity is important as micromanipulation tasks can vary between several millinewtons [2] and a few nanonewtons [1]. Similarly, easy exchange of the end-effector is crucial as the type and dimensions of the end-effector depend on the task in hand (for example grasping, electrical probing or injection) and on the scale (see Fig. 2).

* Corresponding author.
E-mail addresses: michal.smreczak@epfl.ch (M. Smreczak), lennart.rubbert@insa-strasbourg.fr (L. Rubbert), charles.baur@epfl.ch (C. Baur).
URL: https://people.epfl.ch/michal.smreczak/ (M. Smreczak), https://www.insa-strasbourg.fr/fr/lennart-rubbert/ (L. Rubbert), https://people.epfl.ch/charles.baur (C. Baur).

https://doi.org/10.1016/j.precisioneng.2021.04.016
Received 16 June 2020; Received in revised form 8 April 2021; Accepted 20 April 2021
Available online 5 May 2021

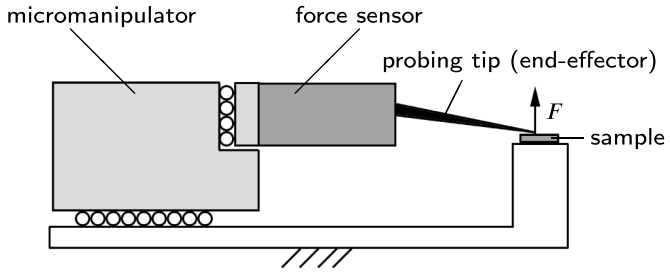

Fig. 1. Schematic of a micromanipulator equipped with a tool holder capable of sensing forces. The end-effector varies depending on the application and may be a probing tip, a micro-gripper or a micro-pipette for example.

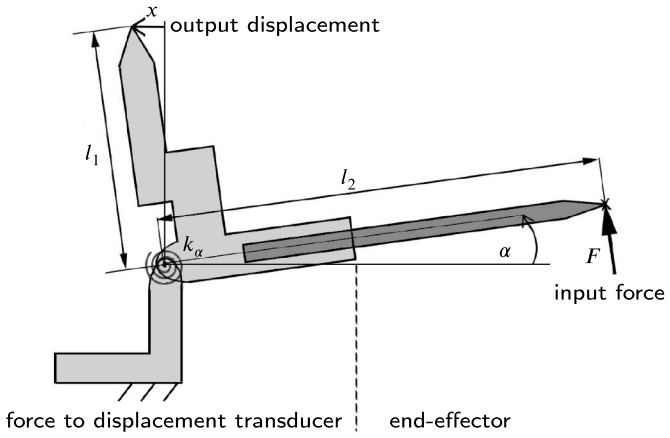

Fig. 2. General principle of the force F to displacement x transformation.

1.2. Current solutions for force sensing at small scales

Various types of end-effectors, depending on the application, can measure force. For example, force can be derived by microgrippers as in Refs. [10,11] where gripping forces are determined with sub-micronewton precision. Other possibilities are conductive probes, as in Ref. [12], to measure micronewton contact forces in electrical nanoprobing. In Ref. [13], micro-pipettes capable of measuring sub-nanonewton forces exerted by cells are presented. In Ref. [14], the authors propose an end-effector dedicated to microscribing and capable of providing small forces in the range of millinewtons onto the surface of material due to low-stiffness flexure implementation. Some applications require other customized end-effectors (e.g. Ref. [2]).

Many studies have been done on the design and development of force-sensing technologies at small scales. As shown in the review [15], the most popular technologies are piezoresistive, capacitive and optical, allowing measurement of forces ranging from millinewtons down to several nano newtons. Other technologies such as electron tunneling [16], the tuning fork [17], inductive [18] and magnetic [19] are possible solutions for force sensing at the micro/nanoscale. In Ref. [20], the sensitivity of the MEMS load cell can be electronically tuned. However, this solution allows adjusting the sensitivity 10 times which is not sufficient for all micromanipulation tasks. In addition, the probing tip is an integral part of the sensor and cannot be easily customized.

A different approach, not requiring the measured force to create strain in the sensor's structure is magnetic levitation. In Ref. [21], the authors present the design of a micro-nano force sensor that because of lack of friction allows force measurement at nanonewton precision. By adjusting the position of the magnets, the sensitivity of the load cell can be adjusted. The main drawback of this solution is its sensitivity to gravity and its own magnetic field, which are undesirable in SEM applications.

This article focuses on force sensing in one direction as in many applications measurement in one axis is key, for example in precise weighing devices, electrical nanoprobing or grasping. Design for single force measurement allows concentrating on the concept validation and avoids challenges from more complex plans, such as fragility and demanding assembly. Nevertheless, some examples from the literature indicate measurement of forces over 2° of freedom (DoF) or 3 DoF as in Ref. [20], and 6 DoF as in Ref. [3]. These solutions require complex structures fabricated as MEMS, which make them fragile, and furthermore they do not provide mechanical stiffness adjustment.

As mentioned above in MEMS, the end-effector is often an integral part of the sensor. One advantage of this approach is compactness and rigidity, as the force sensing part is very close to the probing tip. On the other hand, localization of the sensor close to the probing point may be problematic if multiple probing platforms are used simultaneously and close to one another as in Ref. [22]. Therefore a solution with an interchangeable probing tip, allowing the end-effector's length and shape to be adjusted to the requirements of the specific application, would be advantageous.

Currently, therefore, among all the existing technology, no solution yet provides mechanical stiffness adjustment and a convenient interface for end-effector exchange.

1.3. Advantages of compliant mechanisms for load cells

A load cell is a transducer that converts force (pressure, compression, tension, torque) into a measurable electrical signal [23]. Most of the solutions require that the applied force create a strain in the structure, which is then converted into an electrical signal. As the requirements of load cell design are now widely converging with the advantages of compliant structures, a natural consequence is that force sensing technologies are becoming a major field of flexure development.

Compliant mechanisms, also named flexure mechanisms, are mechanical structures that deform elastically to perform their function [24]. Unlike classical mechanics, they do not have hinges and sliders for their kinematics, but elastic pairs and elastic segments. Reliable models of the most popular elastic pairs and segments are well known [25,26] and allow designing compliant structures with deterministic elastic properties. For more complex mechanisms, finite element analysis (FEA) can be used to obtain a numerical solution of resulting deflection [27].

There are several advantages of compliant joints over conventional hinges. Elastic segments are frictionless, significantly lowering surface wear and heat dissipation. In addition, replacement of classical joints by elastic pairs eliminates backlash which is undesirable in force-sensing applications. Furthermore, machining more complex compliant structures from a single piece of material eliminates a difficult and precise assembly process, which positively affects costs and repeatability of manufacturing. Finally, avoiding the drawbacks of classical joints, compliant mechanisms are very deterministic enabling applying or measuring forces with high resolution and repeatability.

According to Hooke's law, the force applied to a compliant mechanism can be measured as proportional to the elastic deformation of the mechanism. However, force sensitivity of the load cell is not limited by the resolution of the displacement measurement. Several geometrical parameters of the mechanism and the choice of material may affect the displacement with respect to a given force. For example, force sensitivity could be improved by amplifying the output displacement as in Refs. [28,29] or by reducing the overall stiffness as in Ref. [30].

1.4. Stiffness adjustment

Two parameters mainly describe a compliant structure: stiffness and admissible stroke. Stiffness describes the force to displacement ratio. In

the case of force sensing, it is related to the ultimate sensitivity of the load cell. The admissible stroke must be respected to prevent permanent deformation of the structure. In force-sensing design, the measurement range often comes from the admissible stroke. Reducing the overall dimensions of the compliant mechanism results in decreased stiffness, but also limits the admissible stroke. We can avoid this compromise with a stiffness adjustment mechanism, that allows matching sensitivity and measurement range to the specific application. An extensive review of stiffness adjustment methods in MEMS is presented in Ref. [31]. Existing solutions can be divided into passive (mechanical) and active (requiring an actuator) mechanisms. An example of active stiffness control is presented in Ref. [32], where authors adjust the stiffness of a multi-layered beam by changing its temperature. However, the dimensions of multi-layered beams and the need for temperature control make this solution difficult for use in micromanipulation, which often takes place in a vacuum and within a limited space.

One of the passive stiffness adjustment methods is based on the potential energy stored in a preloaded spring. In this way, part of the stored energy can be transferred to the elastic pairs and consequently, they can be deflected with less effort. An example of this approach is the parallel spring stage, equipped with a stiffness compensation mechanism presented in Ref. [33]. In this system, the pre-compressed spring acts on a linear parallel-blade stage, decreasing the overall stiffness to allow sensitivity adjustment. A similar solution is presented in Ref. [34], but the design, validated experimentally by the authors, is larger due to its symmetry. However, using this type of structure for force sensing with adjustable stiffness and for replaceable end-effectors would require static balancing which is more complex for mechanisms with linear motion than rotational. An overview on variable stiffness behavior by virtue of preload forces of selective compliant joints, including rotational cartwheel joints, is presented in Ref. [35]. The ease of static balancing of rotational mechanisms, such as that described in this article, results from the possibility of any displacement of the center of gravity through appropriate adjustment of counter-masses.

In general, compliant joints exhibit positive stiffness. However, the stiffness adjustment mechanism allows decreasing the overall stiffness of the compliant structure to zero, so that the mechanism deflects at a constant amount of energy. In this case the compliant mechanism becomes a zero-stiffness mechanism [36]. Continuing to decrease the overall stiffness results in negative stiffness [37], where the compliant structure works in a bi-stable mode [38]. An example of how the stiffness of a mechanism can be modelled using prestressing forces is [39], in which the authors present a V-shaped negative stiffness structure to compensate for the stiffness of the mechanism.

1.5. Outline of the article

In this article, a novel design of a compliant load cell with adjustable stiffness is proposed. The design can be fabricated at the centimeter-scale, which reduces the fragility, enables mechanical stiffness adjustment, and facilitates interchangeability of end-effectors. Section 2 starts by describing the general concept of the load cell and the way the overall stiffness of the mechanism is adjusted. In section 3, an analytical model of the mechanism is derived. It allows description of the dimensions of a load cell, exhibiting the best-simulated performances. The concept is scale-independent and a methodology for designing the mechanism at different scales is given. Next, experimental validation of the adjustable stiffness mechanism is performed on a demonstrator made of polyoxymethylene (POM). Findings were then used to optimize the parameters and manufacture a prototype made of stainless steel. The course of experiments and parameters of the stainless-steel prototype are described in section 4, followed by the experimental results. To avoid potential problems of precise manipulation and advanced manufacturing, we designed and manufactured the prototype at a significantly larger size than usual for a device performing micromanipulation tasks. For this reason, the article focuses on the static force-displacement behavior of the mechanism and therefore omits the characteristics of dynamics. Thus, the experiments were carried out in a way that excludes oscillations from the measurements. The last section summarizes the findings and details perspectives for the presented solution.

2. General concept

2.1. Conversion of force to displacement

The general idea of the mechanism presented in this article to transform a force into a translation based on a lever coupled pivotably to a fixed frame was first described in Ref. [40]. As an elastic pair composes the pivot, its deflection α is proportional to the torque exerted on the joint, according to Hooke's law. The torque results from the contact force F, normal to the lever, between the probe's tip and the sample. The output displacement x can be thus measured at the opposite end of the lever and equals

$$x = l_1 \sin(\alpha) \tag{1}$$

where

$$\alpha = -\frac{F \cdot l_2}{k_\alpha}. \tag{2}$$

2.2. Overall stiffness and sensitivity

The overall stiffness of the load cell can be computed as the derivative of the input force F function with respect to the output displacement x. As the mechanism exhibits non-linear force-displacement characteristics, the overall stiffness is a non-constant function of the displacement x. To provide an objective measure of the mechanism's stiffness, the overall stiffness k_o is introduced, computed as the tangent stiffness at $x = 0$,

$$k_o = F'(x)|_{x=0} \tag{3}$$

The sensitivity of the load cell is defined as the ratio of the output displacement x to the input force F. As this definition of sensitivity is variable depending on the working point, its value around the zero position will be used to describe the mechanism as displacements are relatively small in micromanipulation applications. For instance, probe tips used in electrical nanoprobing typically have a length of 1–4 cm. In this case, a displacement of $10\mu m$ of the end-effector tip corresponds to less than 1×10^{-6} *rad* of lever rotation. In this article, the value of sensitivity s_0 is the inverse of the overall stiffness k_0 given in (3).

Based on (1)-(2), to increase the sensitivity, lengths l_1 and l_2 should be maximized. In addition, formula (2) shows that an increase in length l_2 is inversely proportional to the measurement range. The limitation of the measurement range comes from the admissible deflection of the compliant joint.

2.3. Stiffness adjustment mechanism

For complex mechanisms with multiple elastic pairs, the potential energy analysis is a convenient starting point for computation of the force. For a simpler illustration of the concept, the stiffness adjustment mechanism is presented in Fig. 3 as an extension of the previously introduced lever.

A linear spring s_l is coupled to the lever by link p and two pivots. The compression of the linear spring equals x_l and can be expressed as

$$x_l(\alpha, x_p) = x_p - \Delta x_l(\alpha), \tag{4}$$

where

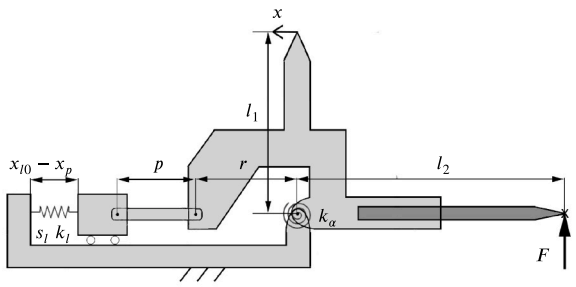

Fig. 3. Ideal joint representation of the stiffness adjustment mechanism.

$$\Delta x_l(\alpha) = r(1-\cos(\alpha)) + p\left(1-\sqrt{1-\frac{r^2\cdot\sin^2(\alpha)}{p^2}}\right) \tag{5}$$

The potential energy of the springs can be computed using formula (6) for the angular spring and (7) for the linear spring.

$$E_{p\alpha}(\alpha) = \frac{1}{2}k_\alpha\alpha^2 \tag{6}$$

$$E_{pl}(\alpha) = \frac{1}{2}k_l\left(\Delta x_l - x_p\right)^2 \tag{7}$$

Thus, the total potential energy of the elastic deformations E_{sum} is the sum of $E_{p\alpha}$ and E_pl and for small α, can be approximated as (8).

The approximation (8) shows that for small deflections α the energy plot for the linear spring s_l has a shape of a negative parabola, which is in opposition to the potential energy of the angular spring. Although the exact form of function (7) makes the energy compensation imperfect for larger deflections, it is possible to obtain precise control of the overall potential energy within a limited range of deflection. Figs. 4–5 present energy plots with different values of x_p, correspondingly for zero overall stiffness and positive overall stiffness.

$$E_{sum}(\alpha) \approx -\frac{1}{2}k_l r^2\alpha^2 + k_l\left(x_p p - p^2\right)\sqrt{1-\frac{r^2\alpha^2}{p^2}} + \\ + k_l p^2 + \frac{1}{2}k_l x_p^2 - k_l p x_p + \frac{1}{2}k_\alpha\alpha^2 \tag{8}$$

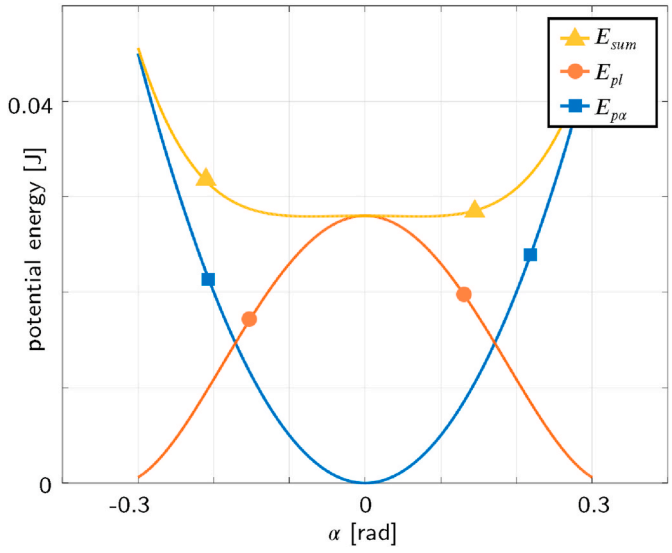

Fig. 4. A zero stiffness case with a constant potential energy for small deflection α. The graph presents potential energy stored in the compliant structure of the stiffness adjustment mechanism. Parameters used to obtain the graph: $k_\alpha = 1$ [Nm], $k_l = 14000$ [Nm], $r = 15$ [mm], $p = 10$ [mm], $x_p = 1.9$ [mm].

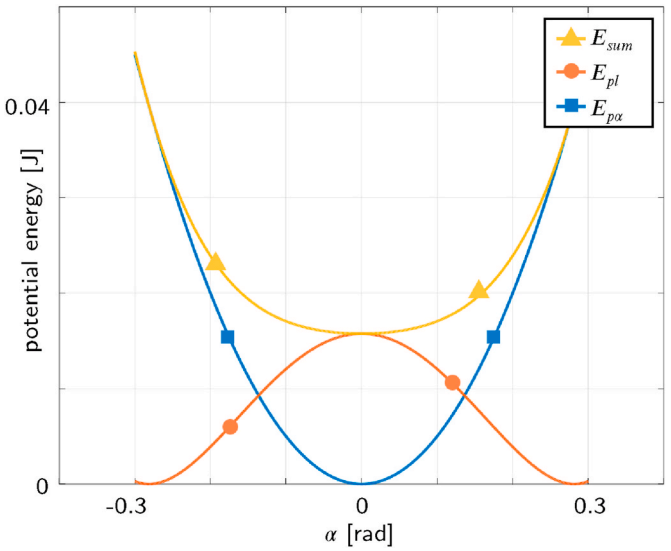

Fig. 5. A positive stiffness case. The graph presents potential energy stored in the compliant structure of the stiffness adjustment mechanism. Parameters used to obtain the graph: $k_\alpha = 1$ [Nm], $k_l = 14000$ [Nm], $r = 15$ [mm], $p = 10$ [mm], $x_p = 1.5$ [mm].

As the potential energy is expressed as a function of angle α, the input force F can be computed as

$$F(\alpha) = \frac{1}{l_2}\cdot\frac{d\,E_{sum}}{d\alpha} \tag{9}$$

The relationship in (1) can be used to obtain the form of $F(x)$ that can be used to plot the force-displacement characteristics of the mechanism, as shown in Fig. 6.

Analytical simulation shows that the stiffness adjustment mechanism allows control of the overall stiffness in a linear fashion as plotted in Fig. 7.

2.4. Linear range of the load cell

The linear range of the force measurement is defined as the range in which the overall stiffness does not change by more than 10% with respect to the overall stiffness measured at $x = 0$. Fig. 8 shows that for a given mechanism, the linear range decreases when the overall stiffness

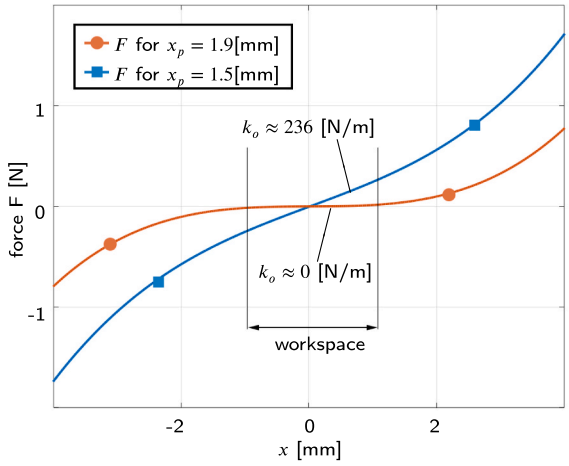

Fig. 6. Force-displacement characteristics obtained from energy plots in Figs. 4 and 5. For relatively small deflection α the characteristic is almost linear which allows the overall stiffness to be determined as slope of $F(x)$.

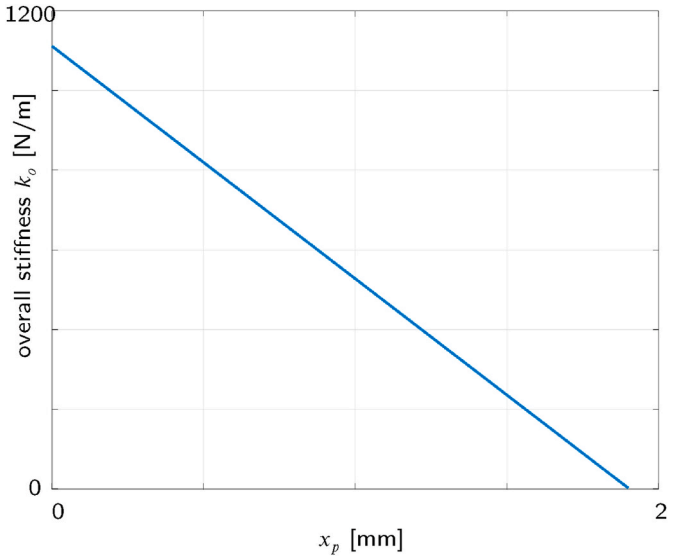

Fig. 7. Overall stiffness k_o as a function of stiffness adjustment displacement x_p. It can be observed that the stiffness adjustment is linear. The plot is generated for $k_\alpha = 1$ [N/m], $r = 15$ [mm], $p = 10$ [mm], $l_1 = 30$ [mm], $l_2 = 30$ [mm] and $k_l \cdot x_p = 14000$ [N/m].

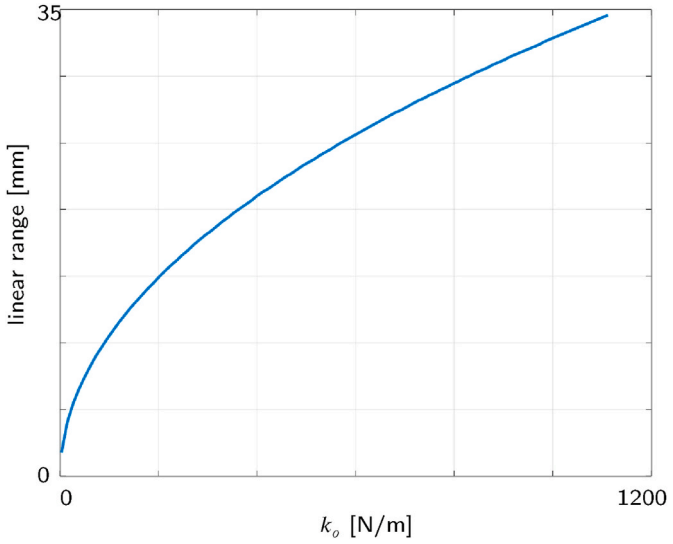

Fig. 8. Linear range as a function of the overall stiffness k_o. The linear range decreases rapidly for near-zero stiffness case. The plot is generated for $k_\alpha = 1$ [N/m], $r = 15$ [mm], $p = 10$ [mm], $l_1 = 30$ [mm], $l_2 = 30$ [mm] and $k_l \cdot x_p = 14000$ [N/m].

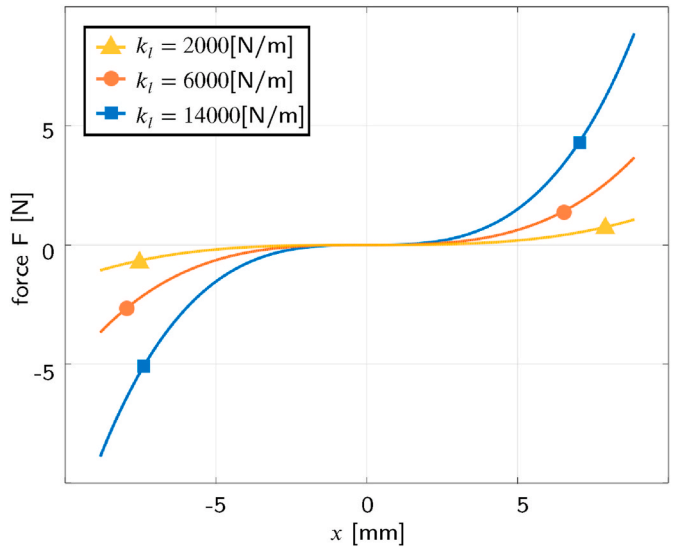

Fig. 9. Modification of stiffness of the linear spring s_l allows adjusting the linear range of the force measurements. Plots are generated for $k_\alpha = 1$ [N/m], $r = 15$ [mm], $p = 10$ [mm], $l_1 = 30$ [mm], $l_2 = 30$ [mm] and a constant pre-compression force $k_l \cdot x_p = 26.66$ [N].

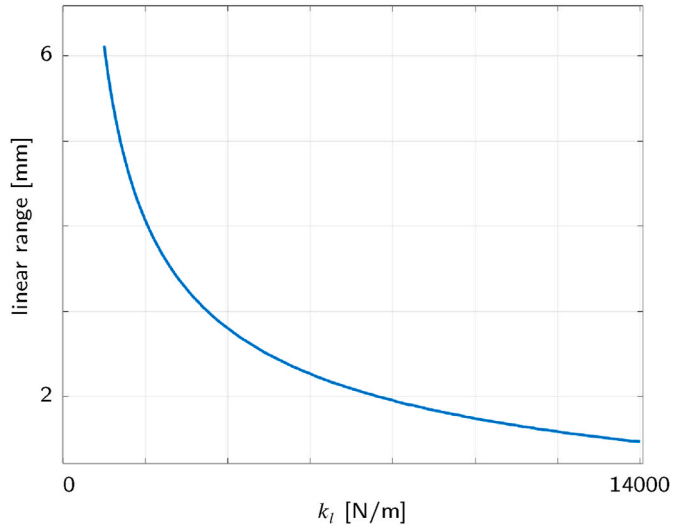

Fig. 10. Linear range as a function of stiffness k_l for constant overall stiffness $k_o = 194.44$ [N/m]. To increase the linear range, stiffness k_l must be minimized. The plot is generated for $k_\alpha = 1$ [N/m], $r = 15$ [mm], $p = 10$ [mm], $l_1 = 30$ [mm] and $l_2 = 30$ [mm].

decreases.

The linear response in the sensor output may be favorable in simple loop-control systems. On the other hand, the nonlinear characteristic of the output signal may be useful to increase the measurement range without loss of sensitivity around the workspace center. The linear range of the stiffness adjustment mechanism can be adjusted by parameters p, r and k_l.

The simplest way to increase the linear range is to decrease the stiffness k_l of the linear spring while keeping the same compression force on that spring (in other words the product of k_l and x_p must be constant). The linear range adjustment by changing the value of parameter k_l is depicted in Figs. 9 and 10.

Dimensions p and r mainly affect the efficiency of the linear spring pre-compression. In Fig. 11 the impact of the dimensions p and r on the overall stiffness is presented. By increasing the r to p ratio it is possible to reduce the compression force on the linear spring, thus reducing its stiffness k_l without the need of increasing the adjustment displacement x_p.

2.5. Gravity compensation

One of the advantages of the presented design is the possibility to attach various end-effectors to the lever. Depending on the type and dimensions of the probe attached to the mechanism, the mass of the probe m_p could unbalance the lever. In order to compensate that mass, an adjustable counter-mass m_a (Fig. 12) may be added, so that

$$m_{l1} \cdot g \cdot \frac{l_1}{2} = m_{lh} \cdot g \cdot \frac{l_h}{2} + m_p \cdot g \cdot \left(l_h + \frac{l_p}{2} \right). \tag{10}$$

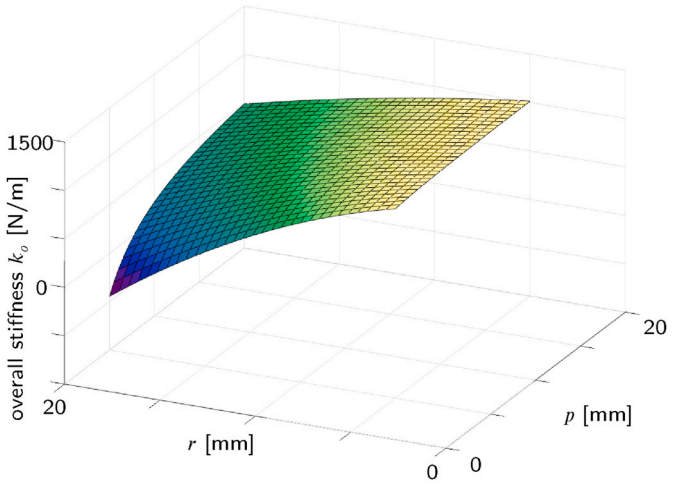

Fig. 11. Overall stiffness of the stiffness adjustment mechanism as a function of p and r. The stiffness is computed for $k_\alpha = 1$ [N/m], $k_l = 14000$ [N/m], $l_1 = 30$ [mm], $l_2 = 30$ [mm] and $x_p = 1$ [mm]. It can be seen that the pre-compressed linear spring reduces the overall stiffness with the highest efficiency when dimension p is minimized and dimension r is maximized.

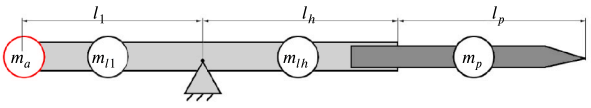

Fig. 12. The mass balance system consisting of an adjustable counter-mass m_a on one of the lever's ends.

As the counter-mass can be used to balance the horizontal mass distribution, analysis of cases where the center of mass is above or below the rotational joint is needed. Depending on the relative vertical position of the center of mass and center of rotation, the three following configurations are possible:

- the center of mass is exactly overlapped by the pivot point (already considered),
- the center of mass is above the pivot point (shown in Fig. 13),
- the center of mass is below the pivot point (shown in Fig. 14).

In Fig. 13, while the force deflects the probe, the center of mass moves down, which results in a decrease in the overall potential energy. Lowering the level of gravitational potential energy affects the overall stiffness, because gravity force helps to deflect the lever. The sum of torques acting on the lever can thus be expressed as

$$T = F \cdot l_2 + m \cdot g \cdot y \cdot \sin(\alpha). \tag{11}$$

As a consequence, the sensitivity of the sensor is increased. An opposing case is presented in Fig. 14. In this case, deflecting the lever results in lifting the center of the mass, which results in an increase in the overall stiffness. The sum of torques acting on the lever is then given as

$$T = F \cdot l_2 - m \cdot g \cdot y \cdot \sin(\alpha). \tag{12}$$

It can be noticed that by designing the center of mass above or below the center of rotation, one can adjust the mechanism's overall stiffness. In addition, attaching an end-effector that displaces the center of mass vertically should be taken into account for precise overall stiffness compensation.

2.6. End-effector replacement

One of the advantages of the mechanism presented in this article is the possibility of achieving a very high sensitivity without needing to reduce its dimensions. As the mechanism should be compatible with different end-effectors, this facilitates the design of the mechanical interface to mount the end-effector and the static balancing overall. Additionally, a larger dimension reduces the fragility of the mechanism and enlarges its rigidity in other directions. With the simultaneous use of mechanical stops and verification by FEM, we can compose the mechanism in such a way that the forces required for manual replacement of the end-effector will not damage the flexures.

The measurements presented in the article are done directly on the mechanism, to be independent of the type of end-effector and to be compared to analytical and numerical simulations. Additionally, it should be noted that the use of a particular end-effector, such as a cantilever, might limit the force measurements to only one direction (by pushing the lever), and additional factors, including surface forces and dynamics, might affect the characterization.

3. Design and analysis of the compliant mechanism

3.1. Ideal joint representation and flexure implementation

The designed load cell mechanism comprises a lever and a stiffness tuning mechanism as described in the previous section. In addition, an adjustment displacement part was implemented allowing control of the parameter x_p, to provide a convenient way of adjusting the overall stiffness. In order to assure maximum precision and frictionless movement, rotational joints b and c are also implemented by flexures. Accordingly, two additional stiffnesses k_β and k_γ have to be taken into account in the analytical modeling. The complete ideal joint representation of the mechanism with parameter markings is presented in Fig. 15.

The flexures are not subject to shear or torsion and the displacements are small, thus equations based on Euler - Bernoulli beam theory can be used to describe their stiffness. Nevertheless, shortening the blades (also referred to as parasitic effects in Ref. [25]), usually studied for large displacements, is also considered to improve the quality of the model.

To implement rotational joints, remote center compliance (RCC) joints depicted in Fig. 16a and b were used. We added a thickening to the middle of the blades that form the joints to increase the critical force, which is the maximum force applied by the preloaded stage to the RCC joint before it starts to buckle. Without the thickening, the value of the critical force was analytically determined as 35.6 N, after adding the thickening, the value equals 119.6 N. At the same time, the thickening increased the stiffness of the RCC joint by only 24%. This variation of an RCC joint with thickening was previously examined in Ref. [41]. For the RCC pivot joint, the angular stiffness k_Θ can be computed as shown in (13). Another important parameter is the admissible deflection, which defines maximum deflection followed by plastic deformation of the

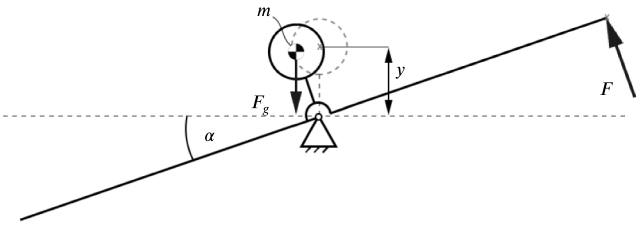

Fig. 13. A lever with a center of mass above the pivot point. In this configuration the overall stiffness of the mechanism is reduced, so the force sensing sensitivity is increased.

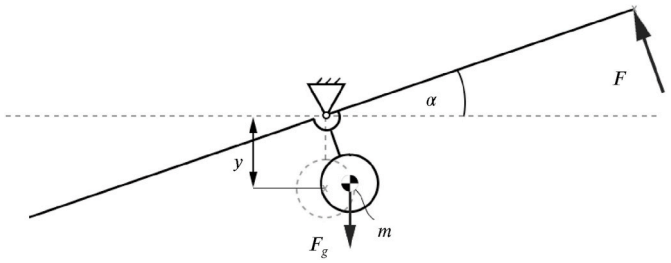

Fig. 14. A lever with a center of mass below the pivot point. In this configuration the overall stiffness of the mechanism is increased, so the force sensing sensitivity is reduced.

structure. Knowing the material and dimensions of the RCC joint, its maximum admissible deflection Θ_{adm} can be computed as in (14). The deflection of an RCC compliant pivot introduces a parasitic shift $\overrightarrow{OO'}$ of its center of rotation. Based on [42], the displacement of the center of rotation can be approximated by (15).

$$k_\Theta = \frac{2EI\left(a^2 + aL + 4\left(L^2 + 3Lq + 3q^2\right)\right)}{(L-a)\left(a^2 + aL + L^2\right)} \tag{13}$$

$$\Theta_{adm} = \frac{2\sigma_{adm}(L-a)\left(a^2 + aL + L^2\right)}{Eh(a^2 + aL + 2L(2L+3q))} \tag{14}$$

$$\left\| \overrightarrow{OO'} \right| = \lambda_\Theta(\Theta) = \frac{4}{60} L \sec\left(\frac{\pi}{4}\right)\Theta^2 \tag{15}$$

where:

E is Young's modulus of the used material.

I is second moment of area for a cross – section, in this case $I = \frac{bh^3}{12}$.

σ_{adm} is endurance limit for 10 million cycles divided by an arbitrary safety factor.

The geometry of the mechanism's frame includes mechanical stops that prevent the compliant joints from exceeding their admissible deflection.

The linear spring used to compensate the overall stiffness is implemented as a parallel spring stage (Figs. 17a-b). This structure constitutes a substitution of a prismatic joint, realized by a slider in classical mechanics. Stiffness k_l and a maximum displacement d_{adm} for a parallel spring stage are presented consecutively in (16) and (17). The stiffness of

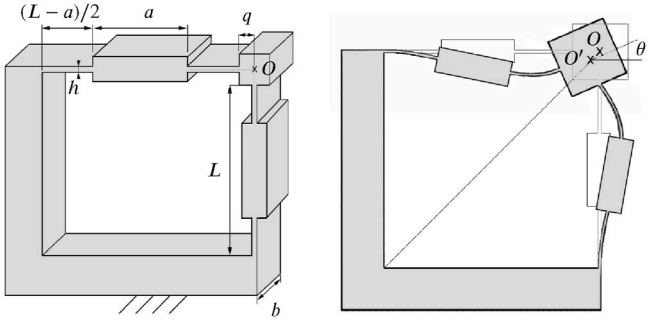

(a) Parametrization of the RCC joint (b) Elastic deformation of the RCC joint

Fig. 16. Remote center compliance flexural joint.

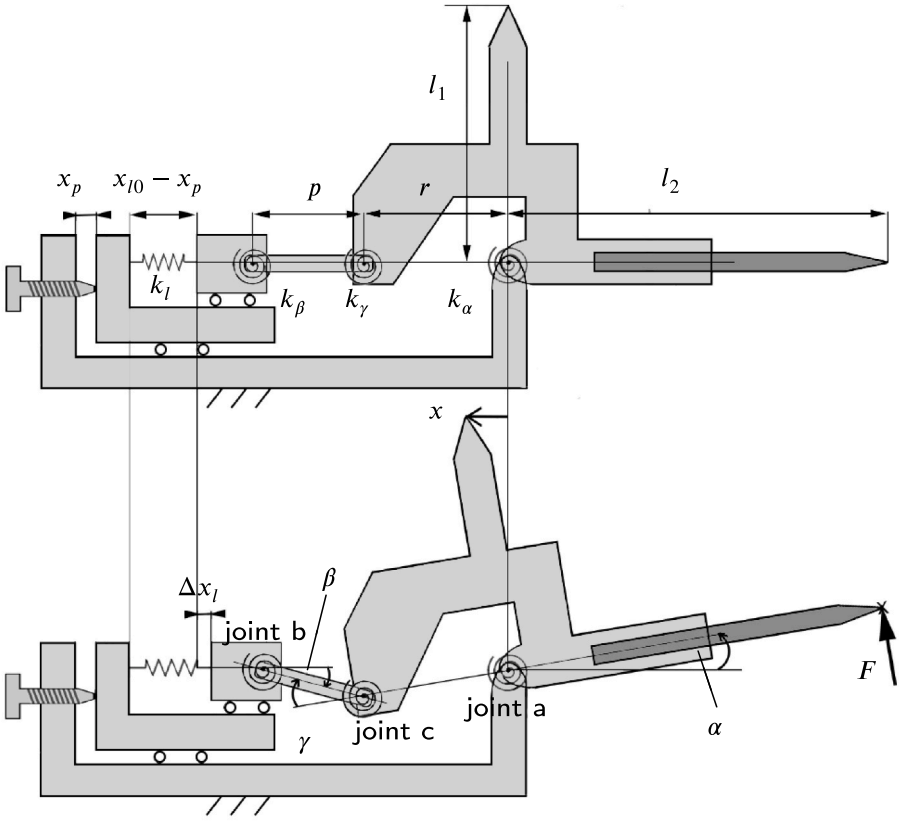

Fig. 15. Ideal joint representation with symbols and parameters used for computations.

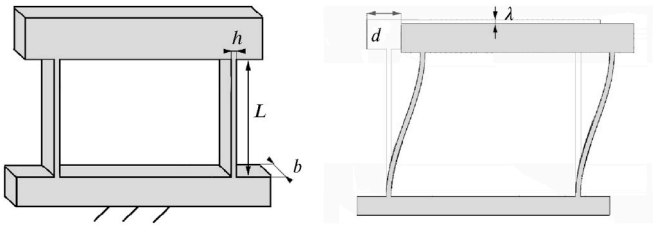

(a) Parametrization of the parallel blade compliant prismatic joint

(b) Elastic deformation of the parallel blade compliant prismatic joint

Fig. 17. Parallel blade compliant prismatic joint.

the joint depends on the number of parallel blade, n. The parasitic displacement $\lambda(d)$ leading to a non-linear course is given by equation (18). Although the mechanism can be realized using either a tensile or compressive spring, the latter option was chosen as the mechanism was meant to be planar and monolithic and at the same time as compact as possible. These design criteria reduce the machining cost and eliminate assembly that might impact the precision of force measurement.

$$k_l = \frac{12EIn}{l^3} \tag{16}$$

$$d_{adm} = \frac{\sigma_{adm} l^2}{3Eh} \tag{17}$$

$$\lambda(d) = \frac{3d^2}{5l} \tag{18}$$

Complete flexure implementation of our mechanism is shown in Fig. 18. The depicted compliant structure is common for the polymer demonstrator, described in 4.1 and the prototype made of stainless steel described in 4.2. The actual dimensions used for designing the load cell in both materials are given in Table 1.

The role of the linear guidance marked in Fig. 18 is to ensure linear movement of the pre-compressed spring and prevent additional degrees of freedom. The guide consists of two parallel blades of the same length as the blades of the pre-compression spring. This ensures that all blades are equally shortened, and parasitic movement is eliminated when adjusting the overall stiffness. The stiffness of the guide has no effect on the performance of the device, as the deflection of the guiding blades is caused by the force exerted by the displacement input. It is important that the compressive force is applied at the center of the blades to avoid additional torque acting on the guiding stage. To prevent guides from buckling due to a slight misalignment of the compressive force, a thickening was added in the middle part of the guiding blades. To dimension the linear guidance accordingly to required stroke and durability, one can use formulas (16)-(18) derived from Ref. [25].

Table 1
Dimensions and parameters used to model and manufacture the demonstrator and the stainless-steel prototype.

Parameter	Demonstrator	Steel prototype
l_1 [mm]	82	82
l_2 [mm]	61	61
p [mm]	30	30
r [mm]	30	30
a [mm]	25	25
q [mm]	5	5
L_a, L_b, L_c [mm]	53	53
k_α [Nm/rad]	0.254	0.618
k_β [Nm/rad]	0.254	0.618
k_γ [Nm/rad]	0.254	0.618
k_{l1} [N/m]	12,861	76,294
n (see (16))	2	5
σ_d [MPa]	40	350
E [MPa]	2500	200,000
x_{adm} [mm]	± 2	± 1.5
$x_{p\ \text{adm}}$ [mm]	2.0	1.1
b(thickness) [mm]	5	2.5

3.2. Analytical model

Implementation of the mechanism by a compliant structure introduces a few more parameters into the analytical model. In addition to equations (6) and (7) derived in 2.3, one has to consider stiffnesses k_β and k_γ in the pivots that couple the linear spring s_l to the lever. Furthermore, flexure implementation of the RCC joints introduces non-negligible parasitic displacements: $\lambda_\alpha(\alpha)$, $\lambda_\beta(\beta)$ and $\lambda_\gamma(\gamma)$. As presented in

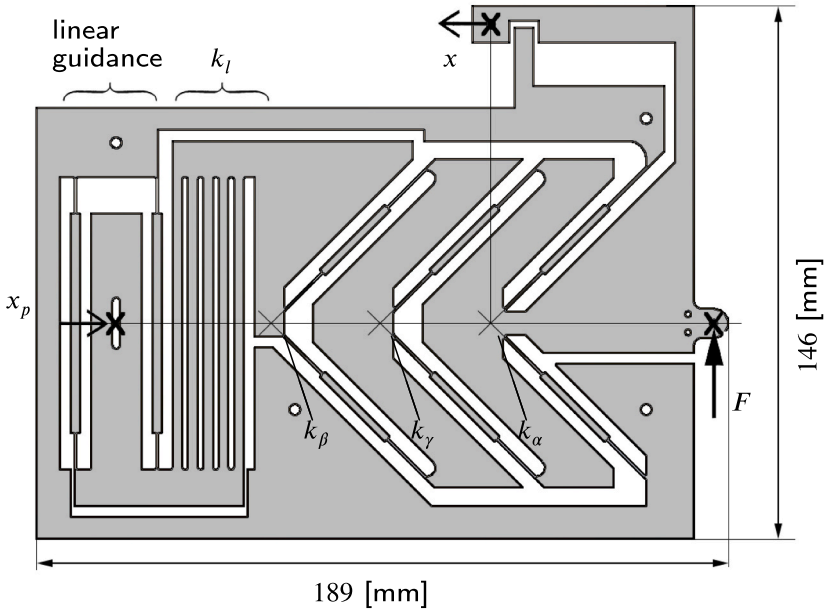

Fig. 18. Flexure implementation of our load cell.

the analytical model, the axes drifts of the RCC joints are used to enhance the efficiency of the stiffness adjustment mechanism. However, the drifts are too small to have a considerable impact on the force measurement accuracy (for a tested rotation, the maximal axis shift of joint a, equals approximately 1 μm). The full equation describing the overall potential energy E_{all} is given as

$$E_{all}(\alpha, x_p) = \frac{1}{2}\Big(k_\alpha \alpha^2 + k_\beta \beta(\alpha, x_p)^2 + k_\gamma \gamma(\alpha, x_p)^2 + +k_l\big(x_l(\alpha, x_p) - \lambda_\alpha(\alpha) - \lambda_\beta(\beta) + -\lambda_\gamma(\gamma)\big)^2\Big) + E_{pg}(\alpha) \tag{19}$$

where

$E_{pg}(\alpha)$ is the gravitational potential energy,

$$\beta(\alpha, x_p) = \arcsin\left(\frac{r \cdot \sin(\alpha)}{p}\right), \tag{20}$$

$$\gamma(\alpha, x_p) = \alpha + \beta(\alpha, x_p). \tag{21}$$

Using formulas (1) and (9) one can obtain the force - displacement characteristic $F(x)$. The overall stiffness k_o is given by (22), where L_a, L_b, L_c are lengths of the blades composing the RCC joints.

$$k_o = -x_p \cdot \frac{k_l\left(\frac{2\sqrt{2}}{15}(L_b r^2 + L_c(p+r)^2 + L_a p^2) + p^2 r + p r^2\right)}{l_1 l_2 p^2} + + \frac{k_a p^2 + k_\beta r^2 + k_\gamma (p+r)^2}{l_1 l_2 p^2} \tag{22}$$

One can observe that for the prototype described in section 4, $r = p$ and $L_a = L_b = L_c$, which simplifies the equation to the form

$$k_o = -x_p \cdot \frac{2k_l\left(p + \frac{2\sqrt{2}}{5}L_a\right)}{l_1 l_2} + \frac{k_\alpha + k_\beta + 4k_\gamma}{l_1 l_2}. \tag{23}$$

4. Experimental results

4.1. Model verification by a demonstrator

The main objective of manufacturing the polymer demonstrator was to have a quick and low-cost verification of the stiffness-adjustment principle. The demonstrator (Fig. 18) was cut from the 5 mm-thick sheet of POM. The experimental determination of force-displacement characteristics (Fig. 19) shows the ability to reduce the overall stiffness to near-zero level and beyond. The material used to manufacture the demonstrator brings in drift and hysteresis to the results; therefore, detailed investigation of the demonstrator was not performed. Proven ability to control the overall stiffness of the mechanism was sufficient to go on to design a stainless-steel prototype.

4.2. Design of the stainless-steel prototype

The prototype was laser cut from a 2.5 mm-thick sheet of stainless steel, except for the RCC pivots, which were machined by electrical discharge machining (EDM). Compared to the polymer demonstrator, only the dimensions of the compliant joints were modified with the new material. Table 1 shows the final key dimensions of the prototype. Before production of the prototype, it was verified by FEM that a thickness of 2.5 mm provided sufficient stiffness for safe assembly and manual manipulation of the prototype. The resistance to non-axial forces acting on the end-effector was also tested. For smaller mechanisms, a thickness of a few millimeters is not a problem for wire-EDM machining, but the mechanism can be further mechanically constrained to prevent buckling or plastic deformation.

4.3. Test bench

The force and displacement measurements were performed on the prototype using the test bench depicted in Fig. 20.

To measure the input force, a reference load cell Kistler 9205 connected to a controller NI Rio was used. The RMS noise of the force measurement consists of a background noise of the reference load cell and the controller, and was determined as 1 mN. The reference load cell was mounted on a 3-DoF manual micro-positioning stage. One axis was used to displace the reference load cell towards the lever of the tested mechanism, thus exerting on the structure the input force F. The two other axes were used for fine positioning of the reference load cell after assembly. The reference load cell was attached to the lever of the tested mechanism by a flexible blade to avoid exerting transversal forces on the sensor. The output displacement x was measured by a laser distance meter LK-H152 with a precision of 0.1 µm. The tested mechanism was mounted horizontally to limit the impact of gravity on the results. Both sensors were set to a sampling rate of 100 Hz. The overall stiffness of the load cell was adjusted by displacing a micro-positioning 1 DoF manual stage.

4.4. Testing strategy

The main objective of the measurements was to determine the overall stiffness k_o of the prototype in a function of the stiffness adjustment displacement x_p. To achieve that, force-displacement characteristics $F(x)$ were plotted for multiple values of displacements x_p.

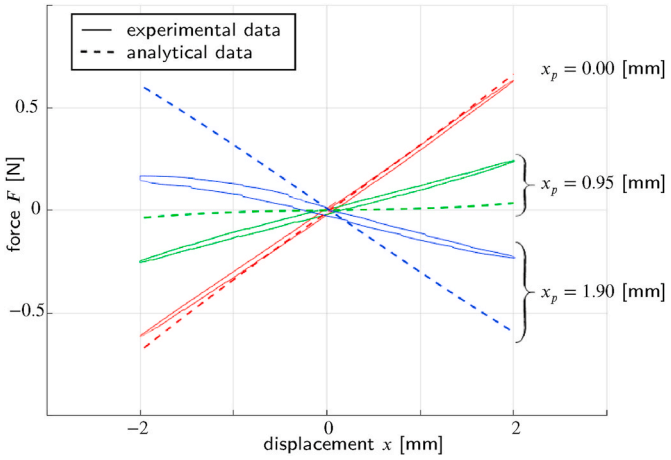

Fig. 19. Force-displacement characteristics for different stiffness adjustments of the polymer demonstrator. Analysis of results allows concluding that adjustment displacement has a visible impact on the overall stiffness and allows reducing stiffness close to zero-stiffness state and beyond, to negative stiffness.

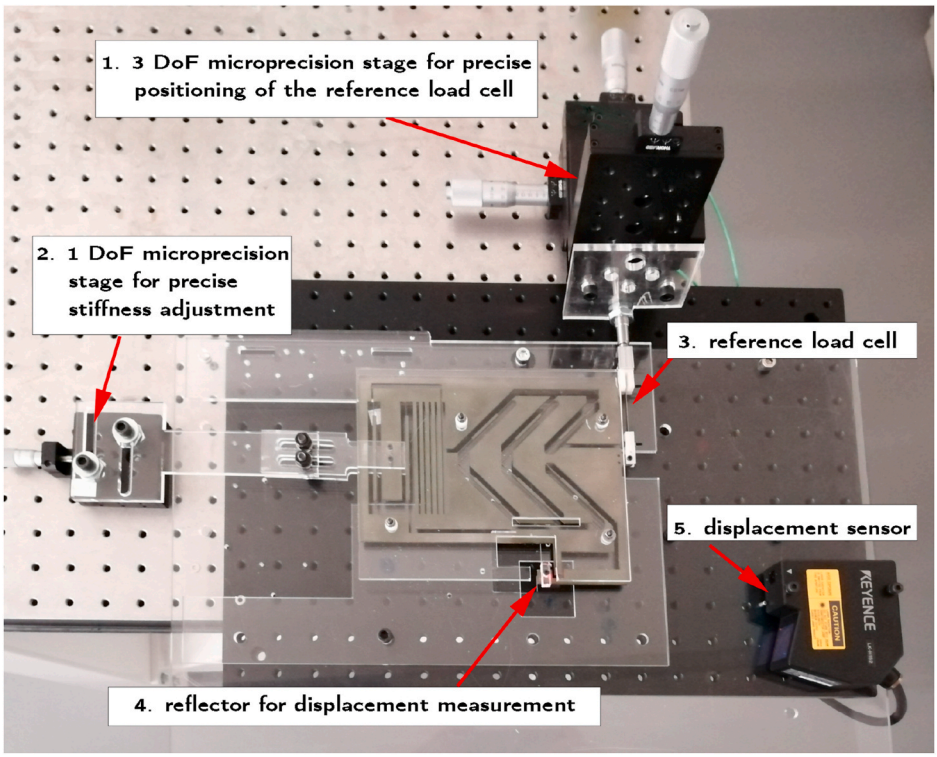

Fig. 20. A view of the test bench used for characterization of the stainless steel prototype. The input force F measured by the reference sensor (3) is applied by displacing the microprecision stage (1). The output displacement x is measured on the reflector (4) by the displacement sensor (5). The overall stiffness of the load cell is adjusted by the microprecision stage (2).

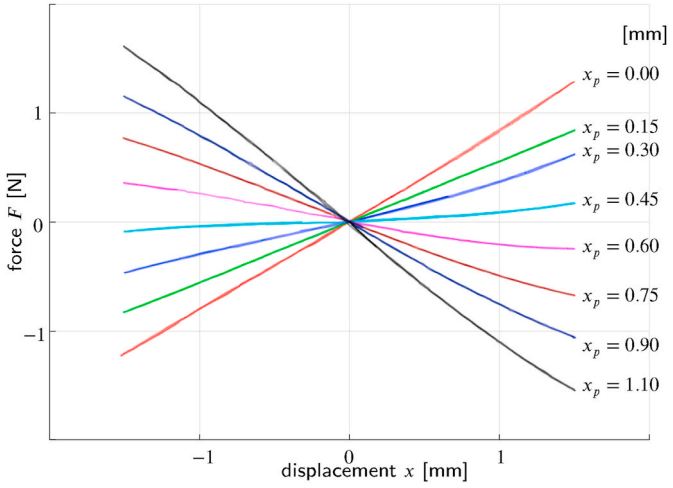

Fig. 21. Force-displacement characteristics measured on the prototype, for different adjustment displacements x_p. The possibility of reducing the overall stiffness to near-zero and beyond, reaching negative stiffness has been demonstrated.

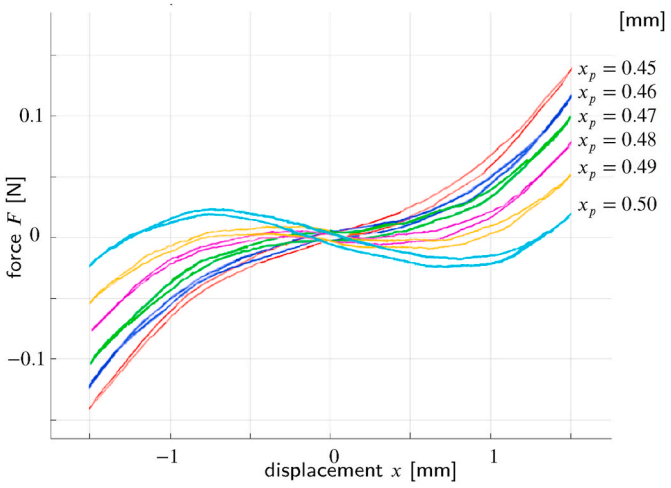

Fig. 22. Force-displacement characteristics measured on the prototype for different adjustment displacements x_p. Near-zero stiffness is obtained for $x_p = 0.48\ mm$.

During the movement of the lever, the output displacement x was recorded by the laser reflected from the counter-part of the lever. For each displacement x_p, the measurements were repeated several times in both directions to observe repeatability and potential hysteresis. Results from all repetitions are superimposed in Figs. 21 and 22.

4.5. Results

The force-displacement characteristics $F(x)$ obtained from the experiments are presented in Figs. 21 and 22.

The force-displacement curve for $x_p = 0\ mm$ shows that the maximum measurement range for the structure is approximately $\pm 1.2\ N$. This value could be increased by preloading the linear spring in

tension ($x_p < 0$), but the purpose of this article was to show the ability to measure small forces for micromanipulation applications. When $x_p = 0\ mm$, the measured sensitivity s_0 equals $1.236 \times 10^{-3}\ m/N$, and overall stiffness k_o equals $809\ N/m$. The force sensing resolution of the tested mechanism can be defined as the smallest change of the input force that can be detected by the mechanism. Therefore, its value depends on the resolution of the displacement sensor, and for $x_p = 0\ mm$ it is equal to $80.9 \times 10^{-6}\ N$.

Near-zero stiffness is obtained for an adjustment displacement $x_p = 0.48\ mm$. For this setting, $s_0 = 0.241\ m/N$ which corresponds to the force sensing resolution of $0.41 \times 10^{-6}\ N$. The overall stiffness k_o measured when $x_p = 0.48\ mm$ is equal to $4.15\ N/m$. These results show potential for further improvement in future research, as the precision of setting x_p was limited by the manual micro-positioning stage. Moreover, it should be noted that using more rigorous displacement sensing technology, such as interferometry-based or capacitive, might allow measuring smaller forces due to their nanometer resolution.

Hysteresis visible in Fig. 22 results from the drift of the piezo-electric reference load cell. In the present case, the achieved force sensing precision is sufficient for characterizing the stiffness adjustment mechanism, however, the use of a more precise reference load cell should be considered in the calibration of the tested mechanism.

The nonlinearity of the force-displacement characteristic does not have a significant impact on the accuracy of the measurement of small forces around zero stiffness due to the possibility of analytical modeling and subsequent compensation of the phenomenon by prior calibration. Additionally, the force-displacement characteristics depicted in Fig. 22 were plotted for a relatively large range of motion, ± 1 mm. In micromanipulation, this range is typically of the order of tens of micrometers, which significantly reduces the impact of nonlinearity on the force measurements.

Fig. 23 presents the overall stiffness k_o as a function of the stiffness adjustment displacement x_p. The results of the numerical simulation are in accordance with the analytical model for $x_p < 0.6mm$, while for large linear compression of the spring there are differences between the analytical and numerical models. The approximation on the Euler-Bernoulli beam theory that assumes constant stiffness and small deformations of the joints explains this difference. The experimental results are consistent with the theory for small x_p, but for $x_p > 1mm$ the error increases to about 20%. The manufacturing precision is the main reason to explain this difference. In fact, we observed heterogeneity in the thickness of the compliant joints, especially for the linear spring which was laser cut. For this phase of our research, we considered that the compromise on manufacturing quality was acceptable to produce a large scale prototype at lower costs and easily testable in our laboratory. In the next phase, the mechanism will be redesigned at a smaller scale and manufactured with enhanced precision to allow for more accurate measurements.

During the experiments, the prototype was fixed to a reference load cell which dampened possible oscillations of the lever. Therefore, the noise level of the force-displacement characteristics corresponds to the noise level of the reference load cell, and dynamic properties of the tested mechanism had no influence on the measurements. In addition, precision of the stiffness determination was limited by the drift in the reference force measurements. Indeed, the reference load cell was identified as the main limiting factor for static characterization of the device at the highest possible precision. As a next step, the mechanism should be scaled down to meet the requirements of real micromanipulation tasks, and its dynamic properties should be characterized.

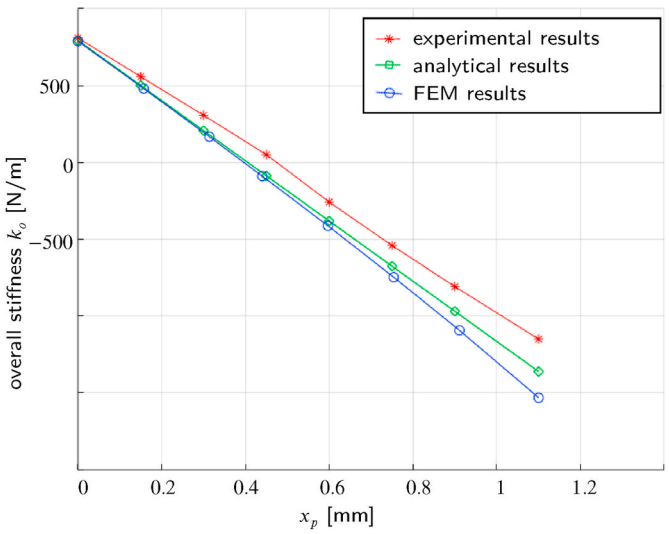

Fig. 23. Overall stiffness k_o as a function of the adjustment displacement x_p- results of experiments on the stainless-steel prototype compared to FEM and data obtained analytically.

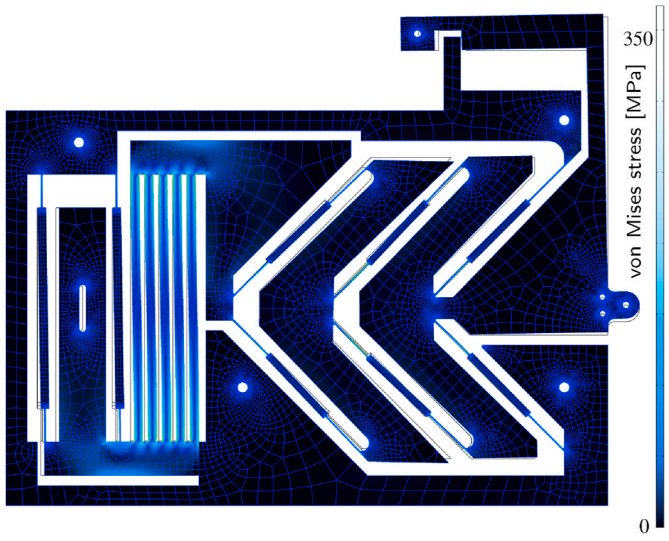

Fig. 24. FEM analysis was performed in software Comsol 5.5. The figure shows the largest von Mises stress in the mechanism that occurs when $x_p = 1.1mm$ and.$x = 1.5mm$

5. Conclusions and perspectives

This article presents a novel design of a compliant load cell with adjustable stiffness. Simulations based on analytical and numerical models (Fig. 24) show the ability to control the overall stiffness of the mechanism and to achieve zero and even negative stiffness. Experiments performed on a stainless-steel prototype enabled us to reduce the overall stiffness to near-zero and beyond, allowing force sensing at levels required by many micromanipulation tasks. Measuring forces from newtons down to micronewtons proved possible with the compliant structure as presented. Of note, improving the resolution of force sensing of the system to nanonewtons is realistic by bringing in the few improvements to the mechanism as discussed above, and by optimizing the vibrations damping. Furthermore, with centimeter-scale dimensions, the load cell's fragility is reduced compared to MEMS solutions, and end-effector interchangeability is facilitated. Finally, as its design is planar and does not require complex assembly process the manufacturing costs are lower.

Our future research is focused on reducing the overall dimension of the load cell to make it compatible with actual micromanipulation setups. Gravity compensation and dynamic properties will also be further investigated.

CRediT authorship contribution statement

M. Smreczak: Conceptualization of this study, Writing - Original draft preparation, Modeling, Experiments. **L. Rubbert:** Methodology, Writing correction, Data analysis. **C. Baur:** Design of the work, Writing correction, Data analysis.

Declaration of competing interest

The authors declare that they have no known competing financial interests or personal relationships that could have appeared to influence the work reported in this paper.

Acknowledgments

The authors would like to gratefully acknowledge the financial support from the European Union's Horizon 2020 research and innovation program under the Marie Skłodowska-Curie grant agreement No 722176).

References

[1] Liu X, Kim K, Zhang Y, Sun Y. Nanonewton force sensing and control in microrobotic cell manipulation. Int J Robot Res 2009;28:1065–76.
[2] Fifanski S, Rivera J, Clogenson M, Baur C, Bertholds A, Llosas P. In: Eu spen ' s 1 6 th International Conference & Flexure-based multi-degrees-of-freedom in-vivo force sensors for medical instruments; 2016. p. 1–2.
[3] Estevez P, Bank JM, Porta M, Wei J, Sarro PM, Tichem M, Staufer U. 6 DOF force and torque sensor for micro-manipulation applications. Sens Actuators, A 2012; 186:86–93.
[4] Eyben P, Vandervorst W, Alvarez D, Xu M, Fouchier M. Probing semiconductor technology and devices with scanning spreading resistance microscopy. New York, NY: Springer New York; 2007. p. 31. https://doi.org/10.1007/978-0-387-28668-6_3. doi:10.1007/978-0-387-28668-6_3.
[5] Bellouard Y. Microrobotics : methods and applications. CRC Press; 2010.
[6] Sitti M. Mobile microrobotics. Cambridge, MA: The MIT Press; 2017. https://mitpress.mit.edu/books/mobile-microrobotics.
[7] Menciassi A, Eisinberg A, Izzo I, Dario P. From "macro" to "micro" manipulation: models and experiments. IEEE ASME Trans Mechatron 2004;9:311–20.
[8] Yang Z, Wang Y, Yang B, Li G, Chen T, Nakajima M, Sun L, Fukuda T. Mechatronic development and vision feedback control of a nanorobotics manipulation system inside sem for nanodevice assembly. Sensors 2016;16.
[9] Shi C, Luu DK, Yang Q, Liu J, Chen J, Ru C, Xie S, Luo J, Ge J, Sun Y. Recent advances in nanorobotic manipulation inside scanning electron microscopes. Microsyst Nanoeng 2016;2:16024.
[10] Fahlbusch S, Shirinov A, Fatikow S. AFM-based micro force sensor and haptic interface for a nanohandling robot. In: IEEE International Conference on Intelligent Robots and Systems, 2; 2002. p. 1772–7.
[11] Piriyanont B, Moheimani SO. Design, modeling, and characterization of a MEMS micro-gripper with an integrated electrothermal force sensor. In: 2013 IEEE/ASME International Conference on Advanced Intelligent Mechatronics: Mechatronics for Human Wellbeing, 2013. AIM; 2013. p. 348–53.
[12] Nafari A, Angenete J, Svensson K, Sanz-Velasco A, Enoksson P. MEMS sensor for in situ TEMnanoindentation with simultaneous force and current measurements. J Micromech Microeng 2010;20.
[13] Sawicka A, Babataheri A, Dogniaux S, Barakat AI, Gonzalez-Rodriguez D, Hivroz C, Husson J. Micropipette force probe to quantify single-cell force generation: application to T-cell activation. Mol Biol Cell 2017;28:3229–39.
[14] Cannon BR, Lillian TD, Magleby SP, Howell LL, Linford MR. A compliant end-effector for microscribing. Precis Eng 2005;29:86–94.
[15] Liang Q, Zhang D, Coppola G, Wang Y, Wei S, Ge Y. Multi-dimensional MEMS/micro sensor for force and moment sensing: a review. IEEE Sensor J 2014;14: 2643–57.
[16] Wang L, Mills JK, Cleghorn WL. Development of an electron tunneling force sensor for the use in microassembly, 1st microsystems and Nanoelectronics research Conference, MNRC 2008 - enabling synergy and Accelerating Excellence in Graduate student research. 2008. p. 205–8.
[17] Giessibl FJ. The qPlus sensor, a powerful core for the atomic force microscope. Rev Sci Instrum 2019;90.
[18] Takenawa S. A soft three-axis tactile sensor based on electromagnetic induction. In: IEEE 2009 International Conference on Mechatronics, 2009. ICM; 2009. p. 1–6.
[19] Praprotnik J, Ergeneman O, Chatzipirpiridis G, Weidlich A, Blaz S, Pané S, Nelson BJ. An array of 2D magnetic micro force sensors for life science applications. Procedia Eng 2015;120:220–4.
[20] Muntwyler S, Beyeler F, Nelson BJ. Three-axis micro-force sensor with sub-micro-Newton measurement uncertainty and tunable force range. J Micromech Microeng 2010;20.
[21] Boukallel M, Abadie J, Piat E. Levitated micro-nano force sensor using diamagnetic materials. IEEE Int Conf Robot Autom 2003;3:3219–24.
[22] Engel JT, Blaikie BE, Kumar A, Castañeda A, Gupta A, Oliver DR. Direct contact four-point probe characterization of Si microwire absorbers for artificial photosynthesis. RSC Adv 2016;6:110344–8.
[23] Muller I, Machado de Brito R, Pereira C, Brusamarello V. Load cells in force sensing analysis - theory and a novel application, Instrumentation and Measurement Magazine. IEEE ASME Trans Mechatron 2010;13:15–9.
[24] Howell LL, Magleby SP, Olsen BM. Handbook of compliant. 2013.
[25] Cosandier F, Henein S, Richard M, Rubbert L. The Art of flexure mechanism design. Lausanne: EPFL Press; 2017.
[26] Howell LL. Compliant mechanisms. Dordrecht: Springer Netherlands; 2016. https://doi.org/10.1007/978-94-017-9780-1_302. doi:10.1007/978-94-017-9780-1_302.
[27] Albanesi AE, Fachinotti VD, Pucheta MA. A review on design methods for compliant mechanisms. Buenos Aires 2010;XXIX:59–72.
[28] Su XPS, Yang HS. Design of compliant microleverage mechanisms. Sens Actuators, A 2001;87:146–56.
[29] Baichapur GS, Gugale H, Maheshwari A, Bhargav SD, Ananthasuresh GK. A vision-based micro-Newton static force sensor using a Displacement-Amplifying Compliant Mechanism (DaCM). Mech Base Des Struct Mach 2014;42:193–210.
[30] Maroufi M, Alemansour H, Bulut Coskun M, Reza Moheimani SO. An adjustable-stiffness MEMS force sensor: design, characterization, and control. Mechatronics 2018;56:198–210.
[31] De Laat ML, Pérez Garza HH, Herder JL, Ghatkesar MK. A review on in situ stiffness adjustment methods in MEMS. J Micromech Microeng 2016;26.
[32] Gandhi F, Kang SG. Beams with controllable flexural stiffness. Smart Mater Struct 2007;16:1179–84.
[33] Henein S. Conception des guidages flexibles, Collection Meta. Presses polytechniques et universitaires romandes; 2001.
[34] Zhao H, Han D, Zhang L, Bi S. Design of a stiffness-adjustable compliant linear-motion mechanism. Precis Eng 2017;48:305–14.
[35] Mauser K, Hasse A. How to prestress compliant mechanisms for a targeted stiffness adjustment. Smart Mater Struct 2020;29.
[36] Herder JL, Barents R, Wisse BM, Dorsser WDV. Efficiently variable zero stiffness mechanisms. In: 4th International Workshop on Human-Friendly Robotics; 2011. p. 2–3.
[37] Hoetmer K, Woo G, Kim C, Herder J. Negative stiffness building blocks for statically balanced compliant mechanisms: design and testing. J Mech Robot 2010; 2.
[38] Opdahl PG, Jensen BD, Howell LL. An investigation into compliant bistable mechanisms. In: Proceedings of the ASME Design Engineering Technical Conference; 1998. p. 1–10.
[39] Kuppens PR, Bessa MA, Herder JL, Hopkins JB. Monolithic binary stiffness building blocks for mechanical digital machines. Extreme Mech Lett 2021;42:101120.
[40] S. Henein, C. Baur, M. Zanaty, M. Kahrobaiyan, Device for measuring a force exerted on an object, Patent EP 19168414.1, Holder: EPFL, 2019.
[41] Shusheng B, Hongzhe Z, Jingjun Y. Modeling of a cartwheel flexural pivot. J Mech Des Trans ASME 2009;131. 0610101–0610109.
[42] Wittrick WH. The properties of crossed flexure pivots, and the influence of the point at which the strips cross. Aeronaut Q 1951;2:272–92.

Michal Smreczak is currently a PhD student in Instant-Lab at École polytechnique fédérale de Lausanne (EPFL). He obtained his master's degree in Robotics at Wroclaw University of Science and Technology, Poland, in 2017. His academical research is oriented towards microrobotics, compliant mechanisms and force sensing technologies.

Lennart Rubbert is currently an associate professor in the department of mechanical engineering at National Institute of Applied Sciences (INSA) in Strasbourg since 2015. He obtained his PhD degree in Robotics at University of Strasbourg in 2012. In years 2013–2015 he worked in a post-doc position in Instant-Lab at École polytechnique fédérale de Lausanne (EPFL). In 2017 he became editor and co-author of the book "The Art of Flexure mechanism Design".

Charles Baur - works as a senior scientist in Instant-Lab at École polytechnique fédérale de Lausanne (EPFL). He obtained his PhD degree in Microtechnology at EPFL in 1992. He has a wide experience in projects related to compliant structures and medtech.